Available online at www.sciencedirect.com

SciVerse ScienceDirect

Geochimica et Cosmochimica Acta 93 (2012) 129–142

Geochimica et Cosmochimica Acta

www.elsevier.com/locate/gca

Retention of inherited Ar by alkali feldspar xenocrysts in a magma: Kinetic constraints from Ba zoning profiles

Paul R. Renne [a,b,*], Sean R. Mulcahy [b], William S. Cassata [a,b], Leah E. Morgan [b], Simon P. Kelley [c], Leslea J. Hlusko [d], Jackson K. Njau [d,e]

[a] Berkeley Geochronology Center, 2455 Ridge Road, Berkeley, CA 94709, USA
[b] Department of Earth and Planetary Science, University of California, Berkeley, CA 94720, USA
[c] Department of Earth Sciences, The Open University, Walton Hall, Milton Keynes MK7 6AA, UK
[d] Department of Geological Sciences, Indiana University, Bloomington, IN 47405, USA
[e] Human Evolution Research Center, University of California, Berkeley, CA 94720, USA

Received 10 April 2012; accepted in revised form 28 June 2012; available online 15 July 2012

Abstract

$^{40}Ar/^{39}Ar$ dating of volcanic alkali feldspars provides critical age constraints on many geological phenomena. A key assumption is that alkali feldspar phenocrysts in magmas contain no initial radiogenic ^{40}Ar ($^{40}Ar^*$), and begin to accumulate $^{40}Ar^*$ only after eruption. This assumption is shown to fail dramatically in the case of a phonolitic lava from southern Tanzania that contains partially resorbed xenocrystic cores which host inherited ^{40}Ar manifest in $^{40}Ar/^{39}Ar$ age spectra. Magmatic overgrowths on the xenocrysts display variable oscillatory zoning with episodic pulses of Ba enrichment and intervals of resorption. Ba concentration profiles across contrasting compositional zones are interpreted as diffusion couples. Inferred temperature time histories recorded by these profiles reveal significant variations between phenocrysts. Combined with Ar diffusion kinetics for alkali feldspars and magma temperature inferred from two feldspar thermometry, the results indicate that >1% inherited ^{40}Ar can be retained in such xenocrysts despite immersion in magma at ~900 °C for tens to >100 years. In cases where the age contrast between inherited and magmatic feldspars is less pronounced, the age biasing effect of incompletely degassed xenocrysts may easily go undetected.

1. INTRODUCTION

Alkali feldspars are prized for dating volcanic extrusions by the K–Ar and $^{40}Ar/^{39}Ar$ techniques because their high K concentrations generate measurable radiogenic ^{40}Ar ($^{40}Ar^*$) accumulations even on the ka timescale (Renne et al., 1997; Quidelleur et al., 2001). It is generally understood that cognate feldspars, once saturated, do not accumulate $^{40}Ar^*$ while immersed in magma due to the high diffusivity of Ar in feldspars at typical magmatic temperatures (i.e., >700 °C). Whether or not xenocrystic feldspars may retain $^{40}Ar^*$ through magmatic processes is not well known because magma residence times are typically poorly constrained. Examples are known wherein this is inferred to be the case for plagioclase due to the brevity of xenocryst entrainment, magma residence and eruption processes (Singer et al., 1998; Layer and Gardner, 2001), but we are unaware of documented cases involving alkali feldspars whose magmatic residence time and temperatures are known.

In a pioneering study, Gillespie et al. (1983, 1984) showed that alkali feldspars in granitic xenoliths entrained in a basalt flow were incompletely degassed, but that some domains were completely degassed and/or purged of inherited $^{40}Ar^*$ during recrystallization, enabling the age of their entrainment – hence by implication the extrusion age of the lava flow – to be determined. Although the plausibility of partial inherited $^{40}Ar^*$ retention in such circumstances

* Corresponding author at: Berkeley Geochronology Center, 2455 Ridge Road, Berkeley, CA 94709, USA.
E-mail address: prenne@bgc.org (P.R. Renne).

0016-7037/$ - see front matter © 2012 Elsevier Ltd. All rights reserved.
http://dx.doi.org/10.1016/j.gca.2012.06.029

was established by Gillespie et al. (1982) based on argon diffusion parameters available at the time and reasonable assumptions about the entrainment process, they did not have independent constraints on the time/temperature history of the xenoliths during entrainment.

Rare examples of excess ^{40}Ar hosted in melt inclusions (Esser et al., 1997) and in unidentified sites (Renne et al., 1997) in alkali feldspars are known. Alkali feldspar xenocrysts in tuffs commonly retain inherited $^{40}Ar^*$ (e.g., Renne et al., 1999), but these are generally believed to have been incorporated in late stages of eruption and/or deposition processes, hence to have experienced magmatic temperatures briefly if at all.

This paper presents an example wherein significant amounts of inherited $^{40}Ar^*$ in alkali feldspar xenocrysts were retained after entrainment in a magma. We investigate whether this is consistent with independent constraints on the thermal history of the xenocrysts in the magma. The sample studied is a porphyritic phonolitic lava that crops out in the Ilongo area near Mbeya in southwestern Tanzania, in the general vicinity of the late Neogene Rungwe volcanics (Ebinger et al., 1989). Basement rocks are not well exposed in the immediate area, but presumably belong to the Ubendian shear belt, which formed episodically between 2100 and 1725 Ma, and was locally reactivated by Pan-African tectonism at ca. 750 Ma (Lenoir et al., 1994).

2. SAMPLE CONTEXT, PETROGRAPHY AND GEOCHEMISTRY

The lava flow sample upon which this study is based was collected in the course of an inventory of potential paleontologic resources by the Tanzanian International Paleoanthropological Research Project (TIPRP) (Njau and Hlusko, 2010). The lava was sampled at Lat. S 8° 47′ 41.2″, Long. E 33° 46′ 10.6″, at 1218 m elevation. The flow is poorly exposed and surficially weathered, and its thickness is estimated at 3 m.

The lava is highly porphyritic, with alkali feldspar phenocrysts up to 1 cm (~15%) and smaller phenocrysts of aegirine–augite (~5%), ferro-pargasite amphibole (~1%), plagioclase (<1%) and euhedral titanite (<1%) set in a bluish-gray (where fresh) groundmass. The amphibole phenocrysts uniformly show opacitic oxidation–resorption rims. The felty groundmass comprises alkali feldspar, aegirine–augite, oxides, apatite and devitrified glass.

Many of the alkali feldspar phenocrysts contain irregularly shaped cores of another alkali feldspar or plagioclase. These cores are generally visible in crossed polars through abrupt discontinuities in extinction angles, but are most clearly revealed in backscattered electron images (see below) because the alkali feldspar overgrowths contain distinctly higher Ba than the cores.

X-ray fluorescence data obtained from the Washington State University GeoAnalytical Laboratory are shown in Table 1. Chemical classification of this lava is complicated by the obvious assimilation of xenocrystic feldspars and uncertain extent of major element contamination, and a relatively high potential volatile content implied by the loss on ignition (LOI). In the classification of Le Bas et al. (1986) it is a tephri-phonolite, but the analysis normalized to a volatile-free basis corresponds to a phonolite.

Table 1
XRF data.

Major and minor element oxides (Wt.-%)	
SiO_2	52.33
TiO_2	0.72
Al_2O_3	21.45
FeO*	3.47
MnO	0.18
MgO	0.47
CaO	3.18
Na_2O	7.62
K_2O	5.67
P_2O_5	0.11
LOI	4.32
Sum	99.51
Trace elements (ppm)	
Ni	3
Cr	3
Sc	1
V	43
Ba	2401
Rb	140
Sr	1503
Zr	303
Y	25
Nb	149
Ga	20
Cu	3
Zn	94
Pb	20
La	117
Ce	195
Th	21
Nd	54
U	3

* Total Fe calculated as FeO.

3. $^{40}AR/^{39}AR$ RESULTS

$^{40}Ar/^{39}Ar$ analysis used methods described in Appendix A. Incremental heating of three individual alkali feldspar phenocrysts (samples 34467–01, -02, and -03) produced complex apparent age spectra (Fig. 1a) initially rising monotonically from ca. 10–20 Ma ages for the first 20–30% of the ^{39}Ar released, then increasing erratically for the remainder of each experiment. Maximum apparent ages for individual steps range from ca. 200 Ma to ca. 5900 Ma, and integrated ages for the three crystals are 41.2 ± 0.1[1], 96.9 ± 0.1, and 326.5 ± 0.5 Ma. In view of petrographic observations and electron microprobe results, these age spectra are straightforwardly interpreted to reflect mixing between magmatic feldspar overgrowths and older, incompletely degassed xenocrystic cores. In this interpretation the age of the magmatic feldspar would be approximated by the initial steps at 10–20 Ma.

[1] Uncertainties here and throughout this paper are given at one standard deviation unless otherwise stated.

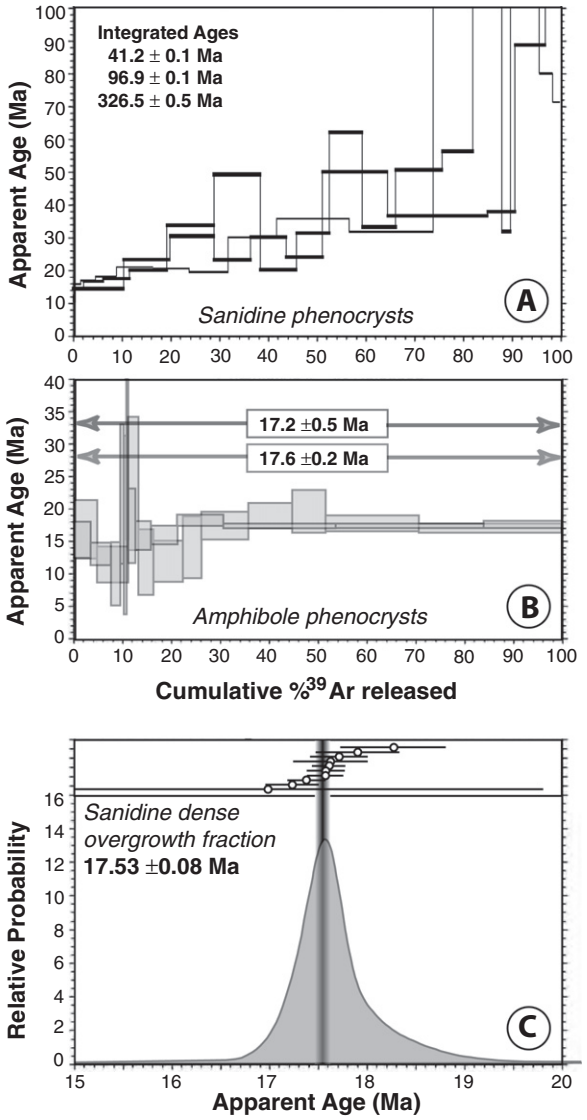

Fig. 1. Continuous laser $^{40}Ar/^{39}Ar$ results. (A) Age spectra for individual sanidine phenocrysts. (B) Age spectra for replicate aliquots of amphibole phenocrysts. (C) Age probability plot for individual dense (Ba-rich) fragments of alkali feldspar overgrowths.

Two multigrain aliquots of amphibole phenocrysts were analyzed by incremental heating. Both yield apparent age plateaus (Fig. 1b) over 100% of the ^{39}Ar released, with indistinguishable plateau ages of 17.2 ± 0.5 Ma and 17.6 ± 0.2 Ma. An isochron fit to all the data from both samples yields an age of 17.9 ± 0.3 Ma, with an atmospheric $^{40}Ar/^{36}Ar$ intercept of 281 ± 9 and MSWD = 0.93.

3.1. Spatial distribution of ^{40}Ar

To test the hypothesis that Ba-poor xenocrystic cores are the source of inherited Ar manifest in the phenocryst age spectra, two strategies were employed.

3.1.1. Physical separation

Several phenocrysts were crushed into small fragments and heavy Ba-rich overgrowths were separated from lighter Ba-poor xenocrysts based on density. Because the Ba substitution has a large effect on the density of alkali feldspars (3.26 g/cm^3 for endmember $BaAl_2Si_2O_8$ versus 2.56 g/cm^3 for endmember $KAlSi_3O_8$), the overgrowth feldspar was concentrated based on the density contrast. Accordingly, alkali feldspar phenocrysts were crushed and sized to a 177–250 micron fraction, then subjected to a heavy liquid separation using dilute Li heteropolytungstate (LST). The densest fraction was analyzed by total fusion of 10 individual crystal fragments. Nine of these proved to be alkali feldspar based on $K/Ca > 10$, whereas one with $K/Ca = 0.056 \pm 0.006$ appears to be plagioclase. All 10 crystal fragments yielded indistinguishable model ages (Fig. 1c) with a weighted mean of 17.53 ± 0.08 Ma, with MSWD = 0.72. An isochron fit to these data yields an age of 17.55 ± 0.13 Ma, with an atmospheric $^{40}Ar/^{36}Ar$ intercept of 280 ± 70 and MSWD = 0.81.

The densest feldspar phenocryst (magmatic overgrowth) fragments and the hornblende phenocrysts yield indistinguishable ages that are interpreted to represent the eruption age of the lava. The atmospheric trapped $^{40}Ar/^{36}Ar$ ratios of both the feldspar overgrowths and the hornblende phenocrysts indicates that whatever inherited "excess" ^{40}Ar existed in the melt was efficiently exchanged with atmosphere prior to eruption. The manifest lack of inherited ^{40}Ar in these phases would seem to preclude inherited ^{40}Ar in the xenocrystic cores being derived via uptake from the melt, a conclusion supported by the very low partition coefficient between alkali feldspars and silicate melts (Clay et al., 2011).

3.1.2. Laser probe analyses

An excimer laser was used to produce 90 μm ablation pits in the surfaces of several feldspar crystals (sample 34,467) and also a traverse across the surface of one crystal (Fig. 2). The resulting flat bottomed pits were around 10–50 μm deep. There was little significant age variation and 17 analyses produced a mean age of 17.74 ± 0.33 Ma. One crystal was subsequently broken to reveal the core

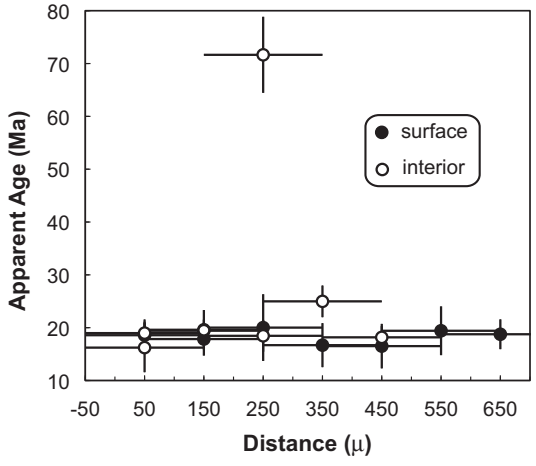

Fig. 2. Laser ablation $^{40}Ar/^{39}Ar$ results for two traverses, one (filled symbols) along the surface of a one grain and one (open symbols) across an interior surface of another grain broken to reveal the core. Uncertainties in traverse distances are ±50 μ.

and two traverses analyzed using the same excimer laser system. In this case two of the eight ages were significantly older, reaching 71.7 ± 1.8 Ma in the core of the grain. Ages in the outer 100 μm of the core fell within errors of the surface ages previously measured. Based on these limited data, the two anomalously old apparent ages near the center of the core are much lower than the oldest apparent ages determined in the incremental heating experiments, suggesting that the laser ablation pits averaged results over a relatively large region relative to the scale of the anomaly.

3.2. Source of excess ^{40}Ar

The eruption age of the lava is straightforwardly deduced from the indistinguishable results of (i) incremental heating of amphibole phenocrysts, and analysis of alkali feldspar overgrowths by (ii) physical separation, and (iii) in situ analysis by laser microprobe. The anomalously old ages derived from the large alkali feldspar phenocryst fragments are clearly associated with lighter, Ba-poor xenocrystic cores that are readily identified petrographically.

This then raises the question of how inherited Ar could be retained rather than lost by diffusion at magmatic temperatures during entrainment and magma residence of the xenocrysts. Addressing this question requires consideration of the specific mode of occurrence of inherited $^{40}Ar^*$ in the xenocrystic cores. If the inherited $^{40}Ar^*$ is distributed in the alkali feldspar lattice, then its retention should be governed by volume diffusion kinetics and the thermal histories of the xenocrysts. If however the inherited $^{40}Ar^*$ is sited in inclusions, as has been inferred in some alkali feldspars (Esser et al., 1997) and plagioclases (Boven et al., 2001; Jones et al., 2008), such inclusions may serve as traps that retard net loss of ^{40}Ar from the composite grains and thereby enhance Ar retentivity. An analogous mechanism was proposed by Shuster et al. (2006) for He in radiation-damaged zones of apatite.

At least some of the inherited $^{40}Ar^*$ in the xenocrysts is clearly parentless as indicated by a presolar apparent age of 5899 ± 67 Ma for one of the incremental heating steps. This observation supports some finite hosting of inherited $^{40}Ar^*$ by inclusions that could act as diffusion traps. Further support for this possibility may be provided by the slightly elevated Cl concentrations (i.e., $^{38}Ar_{Cl}/^{39}Ar_K$) from the older spots analyzed by laser microprobe, although the incremental heating data show no correlation between apparent age and $^{38}Ar_{Cl}/^{39}Ar_K$.

In the following, we address the thermal histories of the alkali feldspar xenocrysts as an independent constraint for evaluating the possibility that volume diffusion failed to quantitatively degas inherited $^{40}Ar^*$.

4. FELDSPAR CHEMISTRY AND XENOCRYSTS

Electron probe microanalysis (EPMA) based on methods described in Appendix B reveals that the overgrowths are generally enriched in Ba, Sr, Ca and Si relative to the cores, and show oscillatory zoning. The contrast between cores and overgrowths, and oscillatory zoning in the latter, are especially evident in backscattered electron (BSE) images (Fig. 3) which are strongly sensitive to Ba concentration. A number of reconnaissance traverses were run across various zones of the alkali feldspar phenocrysts and their cores as shown in Fig. 4. We use the shorthand GxTy to designate traverse y in grain x. In rare cases (e.g., G13 in Fig. 3) the xenocrystic cores are not completely mantled by overgrowths, but are separated from the melt by other phenocrysts, i.e. a clinopyroxene in the case of G13.

In terms of ternary components An–Or–Ab, alkali feldspars and plagioclase are plotted in Fig. 5. Plagioclase data are based on core to rim traverses for two phenocrysts, and a rim–core–rim traverse for a third. Alkali feldspar data, with the celsian (Cn) $BaAl_2Si_2O_8$ component included with An, show that the xenocrystic cores tend to be lower in An + Cn than the overgrowths, but their compositions overlap in this space.

Alkali feldspar phenocryst cores interpreted as xenocrysts are characterized by (i) irregular boundaries (resorption surfaces) and (ii) low Ba (0.01–0.03 atoms per formula unit). As shown by low resolution traverses (e.g., Fig. 6), most crystals show several stepwise increases in Ba from core to rim typically followed by more regular decreases, producing an asymmetric sawtooth pattern. Ba is generally correlated with Ca, Al and Sr, and anticorrelated with Si and K. Among these elements, Ba shows the largest amplitude variations relative to measurement precision, hence its variations are the best resolved and most useful for diffusion modeling.

4.1. Thermometry

Determining magmatic intensive variables for the magma is complicated by the high LOI, manifest xenocryst contamination, and the absence of an appropriate phase assemblage. For example, at 0.1 GPa MELTS (Ghiorso and Sack, 1995) predicts liquidus temperatures of 1131 °C and 945 °C for f_{O2} values at the NNO buffer for the bulk composition (i) recalculated volatile-free and (ii) assigning the LOI entirely to H_2O, respectively. For the bulk composition shown in Table 1, MELTS predicts alkali feldspar of appropriate Or–Ab–An composition at temperatures between 970 and 1030 °C and H_2O concentrations between 0 and 0.8 wt.% at 0.1 GPa and NNO. However, MELTS fails to produce an amphibole or Na–Fe^{3+}-rich clinopyroxene under any of these conditions and the validity of temperatures inferred from phase equilibria by this approach may be questionable. Opacitic rims on the amphibole attest to disequilibrium with the melt upon eruption, but the argon isotopic data betray no evidence of a xenocrystic origin of this phase. The clinopyroxene shows no evidence of resorption or disequilibrium, and we infer that it too is a cognate phase. We conclude that the bulk composition of this lava lies outside the composition space that is well-calibrated for phase equilibria, and we constrain temperatures using two-feldspar thermometry as described below.

Establishing equilibrium between any particular plagioclase composition and a corresponding composition of alkali feldspar is challenging. However, a relatively narrow range of temperatures between 843 and 914 °C is obtained

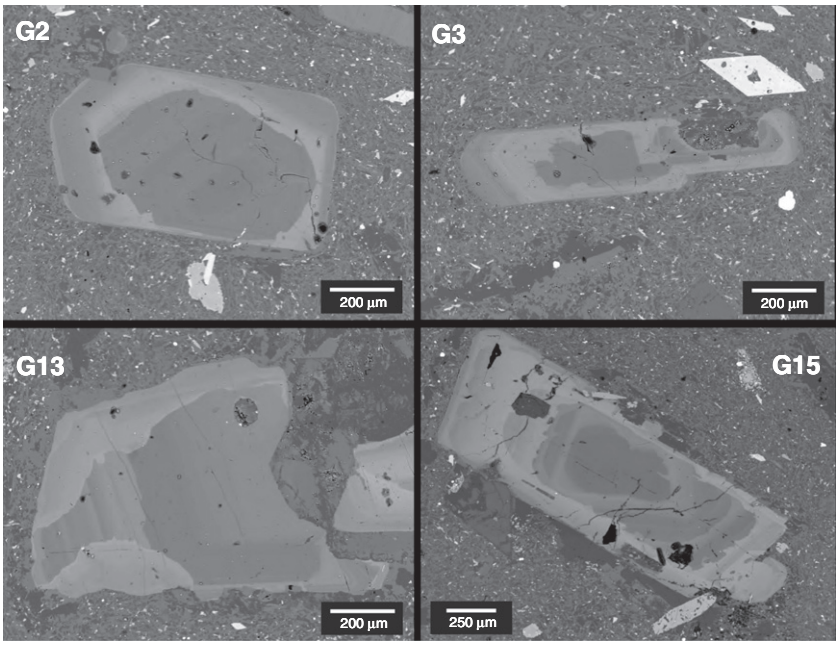

Fig. 3. Backscattered electron (BSE) images of alkali feldspar phenocrysts. Brightness reflects elevated Ba concentrations. Note dark, partially resorbed cores (xenocrysts) in each phenocryst and variably complex zoning in overgrowths.

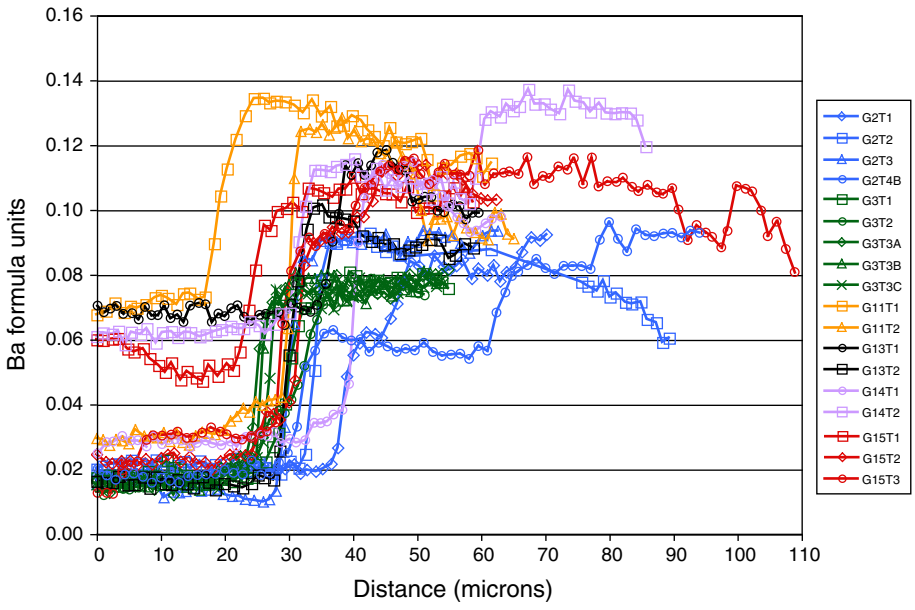

Fig. 4. Ba concentration (atoms per formula unit) in various profiles measured along linear reconnaissance traverses in six different feldspar grains. Traverses are approximately normal to the traces of compositional zone boundaries. All data were acquired with a 15 kV beam. Colors distinguish traverses in a given grain, and different symbols distinguish different traverses. Distance scales for each traverse begin and end at arbitrary positions, but each distance scale increases from interior to exterior portions of the grains. Portions of profiles with <0.03 Ba APFU are from cores (xenocrysts). (For interpretation of the references to colors in this figure legend, the reader is referred to the web version of this article.)

from two-feldspar thermometry (Putirka, 2008) by comparing both core and rim compositions of the plagioclase with the most extreme compositions of alkali feldspar overgrowths. The global regression solution of Putirka (2008), calibrated by 42 experiments, was used. A pressure of 0.3 GPa was assumed based on a geothermal gradient of 30 °C/km and a maximum of 300 °C for partial retention of $^{40}Ar^{*}$ in the xenocrysts. The thermometer is insensitive to pressure between 0 GPa (876 °C) and 1.0 GPa (884 °C). Tests for equilibrium (Elkins and Grove, 1990) yielded

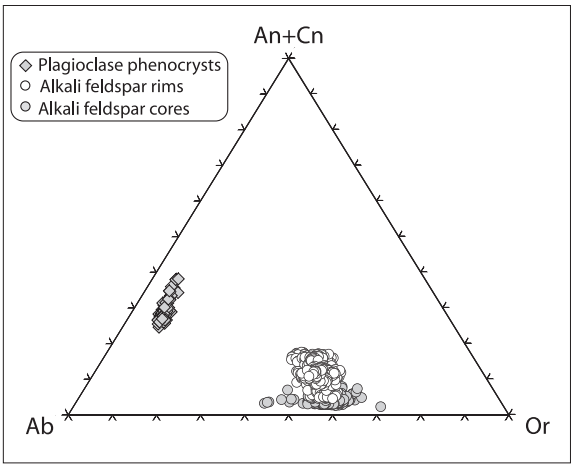

Fig. 5. Ternary representation of feldspar compositions, combining anorthite (An) and celsian (Cn) components, with symbols as indicated.

absolute values of component activity differences between the two phases of <0.45 for An, <0.03 for Ab, and <0.04 for Or. We take the midpoint temperature as a reasonable approximation of the average temperature for alkali feldspar growth, and the extremities of temperature estimates as a conservative approximation to the uncertainty. Thus we infer that alkali feldspar growth (and Ba diffusion across discrete growth zone interfaces) occurred at 879 ± 36 °C, subject to the assumption that high Ba concentrations do not invalidate application of the thermometer.

5. BA DIFFUSION MODELLING

Retention of $^{40}Ar^{*}$ at magmatic temperatures, in light of Ar diffusion data for alkali feldspars (Foland, 1974; Zeitler, 1987; Lovera et al., 1997; Wartho et al., 1999), would seem to require very brief heating of the xenocrysts by the magma prior to eruption. To evaluate the duration of magmatic heating, zoning profiles of trace elements across xenocryst/phenocryst feldspar contacts were analyzed and interpreted as diffusion couples. Our approach is analogous to several previous studies (Nakamura, 1995; Singer et al., 1995; Coombs et al., 2000; Costa et al., 2003; Costa and Chakraborty, 2004; Morgan et al., 2004, 2006; Costa and Dungan, 2005; Morgan and Blake, 2006; Zellmer and Clavero, 2006), which were focused on kinetics of magma processes in arcs and mid-ocean ridge environments. The basis is that initially sharp concentration boundaries between crystal growth zones become relaxed due to diffusion across the boundary in an approach to equilibrium. The extent of relaxation is governed by the time, temperature, and diffusivity of the species in the medium of interest. In the present case, zoning profiles of Ba were particularly useful as Ba concentrations could be measured with reasonable precision and they contrast significantly across the xenocryst/overgrowth contacts; moreover Ba diffusion data are available for alkali feldspars (Cherniak, 2002).

Electron microprobe traverses for major elements, Ba and Sr were conducted using methods described in Appendix B. Contacts between xenocrysts and overgrowths were modeled as diffusion couples wherein the composition across the contact ($x = 0$) is given (Crank, 1975) by:

$$C(x) = \frac{C_1 + C_2}{2} + \frac{C_1 - C_2}{2} erf\left(\frac{x}{2\sqrt{Dt}}\right)$$

where C_1 and C_2 ($C_2 < C_1$) are the initial concentrations on either side of the contact, D is the diffusivity and t is the time duration. For each contact, a least-squares technique was used to solve for the best-fit value of the composite parameter Dt.

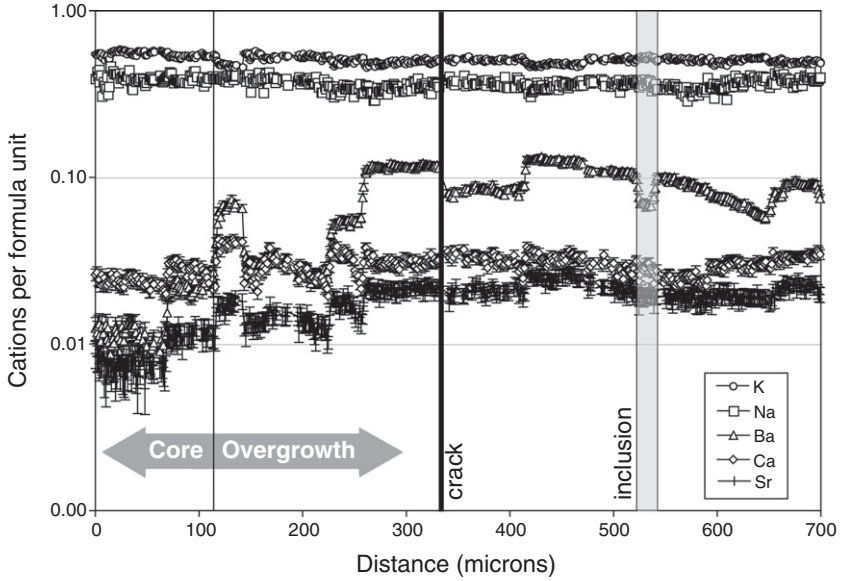

Fig. 6. Core to rim electron microprobe traverse across grain G15 (see Fig. 3) showing variations in Ba, Sr, K, Na and Ca in units of cations per formula unit (eight oxygen atoms).

5.1. Excitation volume effects

For modeling traverse results as diffusion profiles it is important to correct for the excitation volume of the electron beam, which stimulates X-ray emission over a finite region that varies for each element's X-ray lines with material composition and density as well as electron beam energy. The averaging effect across a compositional interface produces a spuriously smooth composition gradient which, unless corrected for, produces overestimation of the extent of diffusion. The effect of varying beam energy for our conditions is illustrated in Fig. 7. For this correction (Ganguly et al., 1988) we used a Monte Carlo estimate (Jercinovic et al., 2008) for the lateral spread of electrons in the sample assuming a linear density-composition relationship along the $BaAl_2Si_2O_8$–$KAlSi_3O_8$ join. Using this approach, a value of $\varepsilon = 0.34$ mm was determined for a 15 kV beam, and $\varepsilon = 0.05$ mm for a 10 kV beam. We used data acquired solely at 10 kV for Ba diffusion modeling.

An additional complication arises when the compositional interface is inclined with respect to the electron beam, i.e. is not perpendicular to the sample surface. If not accounted for, an inclined interface produces bias in the inferred location of the interface and also introduces asymmetry in the shape of the concentration profile, and the magnitude of both of these effects depends strongly on the size of the activation volume (Arnould and Hild, 2003), hence on beam energy as discussed above. For this reason, contacts visibly non-orthogonal to the plane of the thin section were eschewed. Several profiles (e.g., G11T1) yielded discernible asymmetry in Ba concentration profiles suggestive of inclined contacts, and these profiles were not considered for diffusion modeling. Asymmetric profiles may also arise from diffusion-limited initial crystal growth (Solomatov, 1995), further underscoring the need to avoid using such profiles for diffusion modeling.

5.2. Oblique traverses

In order to increase spatial resolution, electron probe traverses were made oblique to the traces of vertical contacts and the results subsequently projected onto an orthogonal traverse. This was accomplished simply by multiplying traverse distance by the cosine of the angle between the traverse and the normal to the interface. Contacts were determined to be vertical within an estimated 10° by noting displacement of the well-defined Becke line upon racking the focus on a petrographic microscope. This approach proved highly effective in increasing spatial resolution without introducing any apparent bias, as shown in Fig. 8. All of the data used for diffusion modeling were acquired using this technique.

5.3. Ba *Dt* values

A test for the validity of the diffusion couple model is that successive contacts between overgrowth zones with sharp Ba concentration contrasts should yield increasing values for the cumulative quantity *Dt* from rim to core provided that the crystals maintain internal thermal equilibrium. Although we assume that the diffusivity is temperature dependent following an Arrhenius relationship, this assumption is not required for the expectation that *Dt* should be cumulative and thus increase inwards from rim to core. This was tested affirmatively with four contacts in G15 that yielded reproducible data with statistically acceptable fits (Fig. 9). These data indicate an initial *Dt* value of $2.7 \pm 0.6\ \mu^2$ at the xenocryst/overgrowth boundary, dropping to $0.4 \pm 0.2\ \mu^2 \sim 300\ \mu$ from the xenocryst margin.

The Ba *Dt* values of greatest interest are those between xenocrysts and the innermost overgrowth layer because these reflect the maximum cumulative duration of heating

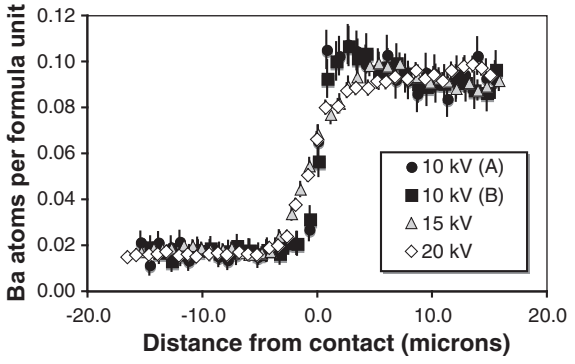

Fig. 7. Effects of varying acceleration voltage on excitation volume in parallel traverses across a contact between core and overgrowth in grain G13. Two traverses (A and B) were made at 10 kV. The larger excitation volume at 15 and 20 kV produces gentler profiles across the contact, spuriously implying more extensive diffusion. Differences in Ba concentration of the overgrowth at ~2–5 mm from the contact are due to lateral variations along the contact. These data were not used for diffusion couple modeling. All data used for diffusion modeling were acquired at 10 kV.

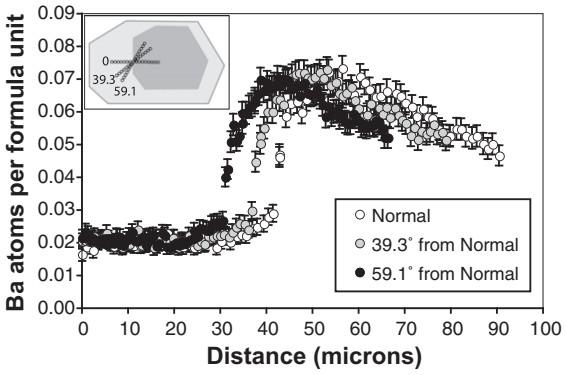

Fig. 8. Effects of varying orientation of traverse relative to trace of interface between cores and overgrowths, measured on grain G15. Relationships are shown schematically in the inset, which shows three traverses in plan view of thin section across a vertical compositional boundary. The highly oblique traverse provides highest spatial resolution. Distances are subsequently projected to orthogonal coordinates. Data used for diffusion modeling were acquired at 59° from normal.

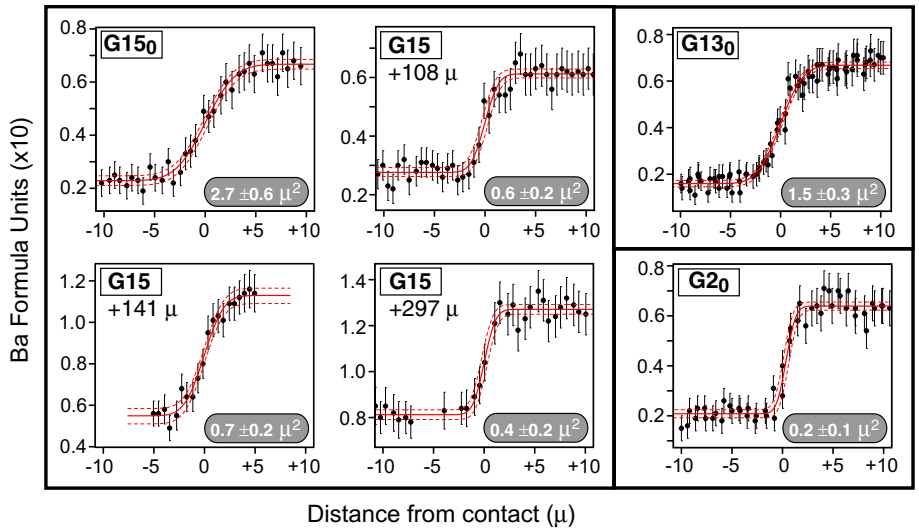

Fig. 9. Electron microprobe traverses (2σ data point errors) across selected boundaries in the grains indicated, shown with least squares fitted diffusion profiles (red curves with dashed error envelopes). Traverses identified with subscripted 0 (e.g., $G15_0$) are from the contact between a xenocryst core and the innermost overgrowth zone. Values of Dt and their uncertainties, computed from the regression and corrected for excitation volume effects, are shown. (For interpretation of the references to color in this figure legend, the reader is referred to the web version of this article.)

of the xenocrysts. Accordingly, detailed traverses across this contact were acquired for several phenocrysts. Ba profiles for three of these met our reliability criteria: (i) symmetric profiles implying subvertical contacts are present; (ii) consistent and unambiguous values of C_1 and C_2 are evident; at least three values intermediate between C_1 and C_2 are present; (iii) multiple traverses across the same contact yield similar results. Data from multiple traverses across each contact meeting these criteria were combined for a single regression.

After correction for excitation volume effects (i.e. subtraction of 0.05 μ^2), grains G2, G13 and G15 yielded values of $Dt = 0.2 \pm 0.1$, 1.5 ± 0.3, and 2.6 ± 0.6 μ^2, respectively. It is noteworthy that the Dt values correlate with the number of distinct overgrowth bands. While three phenocrysts may not be representative of the whole rock, G15 has the most overgrowth layers, and G2 the least, of any observed in thin section. This relationship supports a model wherein the xenocrysts were entrained into the magma episodically, consistent with the heterogeneous zoning patterns discussed below.

5.4. Crystal growth rates

Assuming isothermal conditions and using the diffusion data of Cherniak (2002), these results can be used to estimate diffusion timescales for each contact. Combining these timescales with measured widths of overgrowths between the contacts allows determining average crystal growth rates. At 879 °C deduced from two-feldspar thermometry, the implied growth rate of the innermost 108 μ of overgrowth in crystal G15 is 3.5×10^{-12} cm/s, increasing to 6.4×10^{-11} cm/s for the next 189 μ. These implied rates are consistent with magmatic sanidine growth rates estimated in various studies, which range from 10^{-7} to 10^{-14} cm/s (Long, 1978; Christensen and Depaolo, 1993; Davies et al., 1994; Zellmer and Clavero, 2006; Calzolaio et al., 2010).

5.5. Heterogeneous growth histories

The compositions of successive overgrowths vary between phenocrysts although many discrete compositions are common to several. For example, Fig. 5 shows that crystals G2, G14 and G15 have zones with ~0.06 atoms per formula unit (APFU) Ba; crystals G3, G11 and G13 have zones with ~0.07 APFU Ba; crystals G2, G11, G13 and G15 have zones with ~0.09 APFU Ba; crystals G13, G14 and G15 have zones with ~0.11 APFU Ba; crystals G11 and G15 have zones with ~0.13 APFU Ba.

Similarly, some overgrowth layers are recorded only locally in a given crystal. For example, Fig. 5 shows that G11T1 transects a zone of ~0.07 APFU Ba, whereas G11T2 traverses a contact between a zone with 0.04 APFU Ba and a more rimward one with ~0.12 APFU Ba, without the 0.07 APFU zone present in G11T1. The variable distribution of compositional zones within and between individual phenocrysts may be partly a function of spatially variable nucleation and growth, but to some extent is clearly a preservation artifact due to heterogeneous resorption between growth zones. An extreme case is shown by crystal G13 in Fig. 3.

5.6. Episodic crustal assimilation

The steplike increases in Ba concentration (Fig. 3) in magmatic overgrowths outward from xenocryst cores are clear evidence of discrete pulses of Ba enrichment in the magma. Many of the stepwise composition boundaries between xenocrystic cores and innermost overgrowths, and

between successive overgrowths, are partial resorption surfaces based on their irregular shapes. The slow declines in Ba concentration after each sharp increase are likely the result of progressive Ba depletion in the magma owing to strong partitioning into the alkali feldspar.

Ba partitioning between alkali feldspar and melt is known to be complex, with relatively strong dependence on Or content of the feldspar (Mahood and Stimac, 1990; Icenhower and London, 1996). Our feldspars are typically 50–60 mol-% Or, thus we expect that the partition coefficient to be relatively constant and likely greater than five (Ginibre et al., 2004). Therefore the oscillatory zoning of magmatic feldspar likely reflects magma that was episodically enriched in Ba. In cases where Ba-rich zones grew on resorption surfaces, Ba influx likely accompanied changes in P–T–X conditions in the magma which destabilized the substrate feldspar. We speculate that a likely source of Ba (and water, tending to destabilize feldspars) would be mica-rich crystalline basement rocks given the strong partitioning of Ba into micas relative to other silicate phases (Philpotts and Schnetzler, 1970).

No two of the analyzed crystals show identical zoning patterns. For example, G2, G3 and G15 all show cores with a discrete increase from ~0.2 APFU (atoms per formula unit) Ba followed by large discrete increases to ~0.062, ~0.082, and ~0.071 APFU Ba (respectively). Some overgrowth layers are visibly discontinuous as seen in Fig. 3.

The heterogeneous growth histories presumably reflect spatially and temporally variable Ba concentration in the melt and/or local variations in alkali feldspar solubility such that some layers may have been precipitated and subsequently resorbed in some crystals. Whether this heterogeneity reflects disequilibrium at the scale of a thin section, or late mixing of phenocrysts with disparate prior histories, is unclear.

6. RETENTION OF INHERITED ARGON

We take the value of Dt determined for Ba diffusion across the innermost xenocryst-overgrowth contact in each phenocryst to represent a lower bound on the time–temperature history available for $^{40}Ar^*$ to diffuse out of the xenocryst, as some $^{40}Ar^*$ presumably would have been degassed by conductive heating prior to entrainment. Based on available Ba diffusion data (Cherniak, 2002), Dt values can be translated into square-pulse time temperature–time (T–t) histories as shown in Fig. 10. For comparison, square-pulse equivalent T–t curves are shown for selected fractions of $^{40}Ar^*$ lost by diffusion from the xenocrysts based on the kinetic data compiled by Lovera et al. (1997) for diffusion radii comparable to the dimensions of the xenocrystic cores selected for $^{40}Ar/^{39}Ar$ analysis. The dimensions of cores in the crystals analyzed by $^{40}Ar/^{39}Ar$ incremental heating (e.g., as shown in Fig. 1a) are not known, but cores up to 2 mm are observed and the overall dimensions of phenocrysts selected for the incremental heating $^{40}Ar/^{39}Ar$ analysis were larger than average. More typical are cores of 0.4 to 0.8 mm dimensions, as shown in Fig. 3).

We do not know the specific activation energies (E_a) or pre-exponential factors (D_0) governing Ar diffusion in the xenocrystic cores. Moreover, it is possible that these parameters, as well as any diffusion domain structure initially present in these feldspars, have changed due to structural transformations and/or annealing in response to heating when the xenocryst was entrained by the magma. Given such uncertainty, we considered values of E_a and $\log(D_0/r_0^2)$ one standard deviation from the mean values (46 ± 6 kcal/mol and 5 ± 3 $\log(s^{-1})$, respectively) reported by Lovera et al. (1997), which is the most comprehensive study currently available on Ar diffusion in alkali feldspars and includes data from orthoclase, microcline, and perthite. Ar diffusion experiments using sanidine reported by Zeitler (1987) fall within the range of values reported by Lovera et al. (1997). Thus the data encompass a reasonable range of expected diffusion parameters, although we cannot dismiss the possibility that the feldspar studied herein is more or less retentive. Lovera et al. (1997) suggest a value of $r_0 = 6$ μm as being the most relevant diffusive lengthscale to extracting D_0 from their $\log(D_0/r_0^2)$ data. In modeling diffusive loss from our alkali feldspars crystals we assume the effective diffusive lengthscale (r) for calculating $\log(D_0/r^2)$ from the aforementioned D_0 value is between 250 and 1000 μ, consistent with observations of xenocrystic core and whole-grain dimensions.

Thus, Fig. 10a–c shows results corresponding to the more retentive values ($E_a = 40$ kcal/mol; $\log(D_0/r_0^2 = 2$ $\log(s^{-1})$), and Fig. 10d–f shows results for the least retentive ($E_a = 52$ kcal/mol; $\log(D_0/r_0^2 = 8$ $\log(s^{-1})$). Plane slab diffusion geometry was assumed. For each set of parameters, these results provide a maximum constraint on the fraction of $^{40}Ar^*$ lost because they ignore the additional diffusion distance provided by successive overgrowths on the xenocrysts. The core-overgrowth relationships (based on petrography) appear epitaxial, in which coherent phase boundaries are expected. Hence the margins of the xenocryst cores are not expected to serve as natural diffusion boundaries and the lengthscales of whole phenocrysts are logical maximum diffusion dimensions.

It is noteworthy that the dense overgrowth fragments analyzed by $^{40}Ar/^{39}Ar$ (see Section 3.1.1 and Fig. 1(c)) yielded apparent ages with only minor skew towards older ages. The xenocryst/overgrowth boundaries are expected to be coherent, requiring that inherited $^{40}Ar^*$ diffusing out of the xenocrystic cores must diffuse through whatever overgrowths existed before exiting the phenocrysts. The lack of observed excess ^{40}Ar in the overgrowth fragments analyzed supports the possibility raised by the laser probe data (see Section 3.1.2) that the inherited $^{40}Ar^*$ has a sharply peaked spatial distribution, with peaks in the xenocrystic cores and tails of very low concentrations (into the Ba-rich overgrowths). This would be enhanced by a higher diffusivity of Ar in the Ba-rich overgrowths, which is possible in view of the large range in kinetic parameters observed by Lovera et al. (1997).

It is also noteworthy that all of the xenocrystic cores observed are separated from the innermost overgrowth layer by a resorption surface. If significant $^{40}Ar^*$ was lost from the cores prior to initial overgrowth formation, and if the kinetics of resorption were faster than those of Ar diffusion, as seems likely, the Ar diffusion profiles in the cores would have truncated tails prior to the initial precipitation of

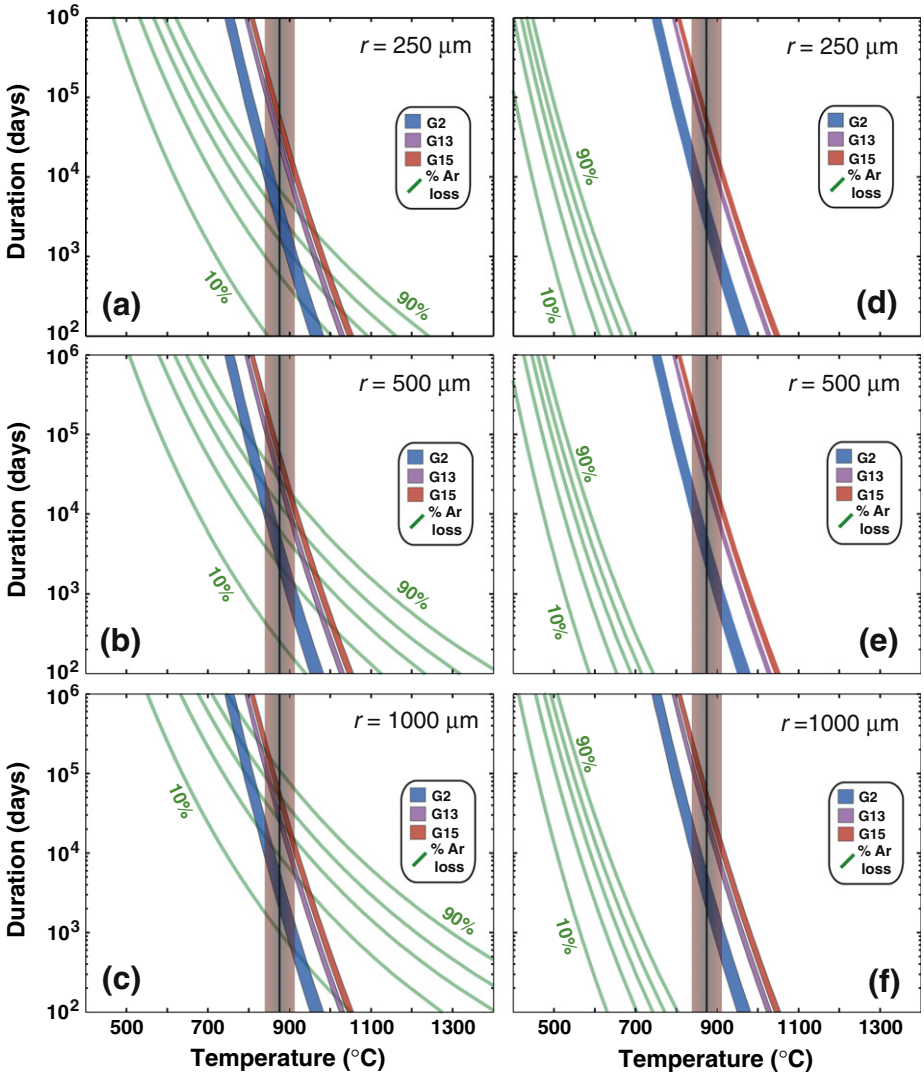

Fig. 10. Permissible time–temperature square-pulse heating scenarios that predict the Ba diffusion profiles (colored bands bounded by error limits) compared with time–temperature square-pulse heating scenarios that predict 10–90% $^{40}Ar^{*}$ loss (green curves; calculated for three different diffusion radii (r) as indicated). The vertical band centered at 879 °C shows the magma temperature and range inferred from two-feldspar thermometry. The intersection of the vertical band (the inferred magma temperature) and the colored bands (the permissible time–temperature histories constrained by the Ba diffusion profiles) defines the magma residence time. The mutual intersection of the two aforementioned bands with a green curve defines the predicted fractional loss of $^{40}Ar^{*}$ due to magma residence. Fractional $^{40}Ar^{*}$ loss curves are calculated from diffusion data summarized by Lovera et al. (1997), with mean values of activation energy ($E_a = 46 \pm 6$ kcal/mol) and pre-exponential factor $\log(D_0/r_0^2) = 5 \pm 3$). Fractional loss curves are shown for diffusion parameters one standard deviation higher and lower than these mean values, representing lower and upper bounds (respectively) on argon retentivity. The fractional loss curves in panels (a–c) correspond to $E_a = 40$ kcal/mol and $\log(D_0/r^2) = 2$. Those in panels (d–f) correspond to $E_a = 52$ kcal/mol and $\log(D_0/r^2) = 8$.

magmatic overgrowth feldspar. Such a scenario would produce an initially sharp discontinuity in $^{40}Ar^{*}$ concentration across the core/overgrowth contact.

Our modeling suggests that none of the T–t histories experienced by grains G2, G13 or G15 are consistent with retention of significant $^{40}Ar^{*}$ if the Ar diffusion parameters ($E_a = 52$ kcal/mol and $\log(D_0/r_0^2) = 8$) 1σ greater than the means of the Lovera et al. (1997) distributions are used, even with diffusion radii at the large end of the plausible range of grain dimensions (Fig. 10d–f). On the other hand, if diffusion parameters ($E_a = 40$ kcal/mol and $\log(D_0/r_0^2) = 2$) 1σ less than the means of the Lovera et al. (1997) distribution are used (which yield lower diffusivities than higher E_a values at magmatic temperatures), a core with the T–t history of grain G2 would be expected to retain as much as 70% of its $^{40}Ar^{*}$ for any diffusion dimension >250 μm, and all three T–t histories could retain >10% of their $^{40}Ar^{*}$ for diffusion dimensions >500 μm. The possible siting of some inherited $^{40}Ar^{*}$ in diffusion traps as discussed previously is thus permitted but not required to explain our results. We reiterate that ascribing constant diffusion parameters to the core feldspars may be an oversimplification as they may have undergone structural changes upon heating in the magma.

The actual fraction of $^{40}Ar^*$ retained or lost from each xenocryst is unknown without information about their original Ar retention age(s). However, reasonable values can be modeled. If the original age was ~2 Ga (Ubendian; Lenoir et al., 1994) the youngest (41.2 Ma) and oldest (327 Ma) integrated ages would correspond to 99% and 90% $^{40}Ar^*$ loss, respectively, assuming instantaneous loss at 17 Ma. If the original age was 750 Ma (Pan-African; Lenoir et al., 1994), these values would be 95% and 60%, respectively. Thus the amount of $^{40}Ar^*$ retained by the xenocrysts is consistent with the integrated ages regardless of the original ages of the xenocrysts, within the wide range of possible argon diffusion parameters.

7. CONCLUSIONS

Inherited $^{40}Ar^*$ is clearly associated with xenocrystic cores within alkali feldspar phenocrysts in the phonolitic lava studied here. The cores unequivocally retained inherited $^{40}Ar^*$ despite immersion in magma at 879 ± 36 °C. Alkali feldspar phenocrysts in a single thin section reveal diverse histories of nucleation on xenocrysts and subsequent growth histories marked by episodic Ba-enrichment in the magma and instability reflected in partial resorption events. Ba diffusion profiles across xenocryst/phenocryst boundaries reveal magma residence times of the xenocrysts ranging from thousands to tens of thousands of days (8–110 years). Based on these constraints, retention of significant and variable fractions of inherited $^{40}Ar^*$ in the xenocrysts is expected for plausible values of diffusion parameters provided that diffusion lengthscales are approximated by physical phenocryst dimensions. These results accord well with the results of incremental heating $^{40}Ar/^{39}Ar$ experiments on individual phenocrysts.

Without knowing the actual Ar diffusion parameters in both core and overgrowth phases, their specific three dimensional geometries, and the initial $^{40}Ar^*$ concentrations of the cores, it is impossible to make more quantitative statements about the expected extent of $^{40}Ar^*$ retention. However, we note that techniques such as X-ray tomography (Ketcham and Carlson, 2001) can quantify three dimensional interior morphologies of crystals. Ba increases X-ray absorption significantly and thus the strong Ba contrasts between cores and overgrowths favors the possibility of mapping core-overgrowth boundaries with this technique. Mapping cores of individual crystals prior to $^{40}Ar/^{39}Ar$ analysis would permit modeling with numerical diffusion codes (Huber et al., 2011) capable of operating on arbitrary geometries. Such approaches would likely be fruitful in cases such as we have explored here.

Inherited $^{40}Ar^*$ in alkali feldspar xenocrysts entrained in lavas is probably not be a ubiquitous phenomenon, but it is probably more common than is widely supposed. The time scale of magma residence inferred for alkali feldspars in some studies (Morgan et al., 2006) is shorter than determined here, thus the present case is not an extreme one. Detection of the effects shown here would be more difficult if the inherited components were only slightly older than the magmatic event mobilizing them, as may be exemplified in alkali feldspar megacrysts in the Fish Canyon Tuff (Bachmann et al., 2007) which yielded slightly but significantly older ages than phenocrysts. Selection of large phenocrysts for $^{40}Ar/^{39}Ar$ dating, commonly employed to maximize measurement precision, is counterproductive in such cases because the retention of inherited $^{40}Ar^*$ is enhanced by an increased diffusion lengthscale.

Finally, we stress that in cases such as this where the fraction of inherited $^{40}Ar^*$ retained is likely very small, uncertainties in Ar diffusion parameters are too large to permit useful constraints on the kinetics of magmatic processes. What we have shown here is that within such uncertainties, and in light of independent constraints posed by Ba diffusion profiles, the observed retention of detectable inherited $^{40}Ar^*$ in alkali feldspar xenocrysts is plausible under some realistic circumstances.

ACKNOWLEDGMENTS

We dedicate this paper to the late Ian S.E. Carmichael. We thank Bill Mitchell for helpful suggestions; Keith Putirka for advice on use of his feldspar thermometry program; Bill Hames, Paul Layer, an anonymous reviewer and Associate Editor Peter Reiners for constructive reviews of the manuscript; NSF (Grants EAR-0838572 and BCS-0321893) for partial support of this research; and the Tanzanian Government (Commission for Science and Technology, and Department of Antiquities) for fieldwork permits.

APPENDIX A. $^{40}AR/^{39}AR$ METHODS

Samples were prepared using standard methods and facilities described elsewhere (Renne et al., 1999). Samples were irradiated in the CLICIT facility of the Oregon State University TRIGA reactor in two batches. The first irradiation, for 5.0 h and using the Fish Canyon sanidine (FCs) standard (Renne et al., 2010), consisted of alkali feldspar phenocrysts 3–4 mm in dimension. The second batch, irradiated for 2.0 h and using the Alder Creek sanidine (ACs) standard (Nomade et al., 2005), consisted of (i) small (177–250 μ) fragments of dense alkali feldspar separated via LST, and (ii) amphibole phenocrysts.

Samples were analyzed in three distinct sets of experiments. Incremental heating and single crystal fusion analyses were conducted at the Berkeley Geochronology Center (BGC), and spot fusion analyses with a UV laser microprobe were conducted at the Open University (OU). BGC and OU data are given in electronic annexes EA-1 and EA-2, respectively.

At BGC, irradiation batch 1 and 2 samples were analyzed with MAP 215C and MAP 215–50 mass spectrometers (respectively), as described previously (Renne et al., 1998). Mass discrimination was monitored by online analysis of air pipettes based on a power law relationship (Renne et al., 2009) which gave $D = 1.00630 \pm 0.00148$ per amu for Batch 1, and $D = 1.00694 \pm 0.00127$ per amu for Batch 2, each based on 29 pipettes interspersed with the unknowns. Radioactive decay of ^{37}Ar and ^{39}Ar were corrected using the decay constants of Renne and Norman (2001) and Stoenner et al. (1965), respectively.

At OU, several grains of one sample were analyzed using a Nu Noblesse mass spectrometer mated to a 193 nm

eximer laser system. Mass discrimination was determined by ablation of a standard glass containing modern atmospheric argon indicating a discrimination factor of 1.0113 per amu.

Ar isotope data, corrected for backgrounds, mass discrimination and radioactive decay are given in Tables EA-1 and EA-2. Apparent ages were computed from these data corrected for interfering isotopes using the production ratios given by Renne et al. (2005, 2008). Ages are based on the calibration of Renne et al. (2010), as updated by Renne et al. (2011).

In the step-heating experiments, the significance of step ages at higher fractional degassing is not obvious. A presolar age of 5899 ± 67 Ma for one step clearly indicates that some of the ^{40}Ar is unsupported, i.e., it is decoupled from parent ^{40}K. We hypothesize that some of the $^{40}Ar^{*}$ degassed from the xenocryst cores diffused into K-poor voids and/or inclusions.

APPENDIX B. ELECTRON MICROPROBE ANALYSIS

Electron probe microanalysis (EPMA) was conducted with a Cameca SX-51 instrument in the Dept. of Earth and Planetary Science at the University of California, Berkeley. The sample was a carbon-coated polished thin section. Data acquisition, analysis, and correction procedures were conducted with the software Probe for EPMA (version 8.48).

Analyses were conducted with a beam current of 10 nA and a beam diameter of 1 μ. The accelerating voltage varied for some experiments as described below. In particular, to explore the effects of activation volume as discussed below, several parallel traverses were run at variable accelerating voltages of 10, 15 and 20 kV. Elements were acquired using the analyzing crystals LIF for Fe ka, Mn ka, PET for Ti ka, Ca ka, K ka, Ba la, and TAP for Al ka, Na ka, Si ka, Mg ka, Sr la. The counting time was 30 s for all elements. The intensity data for Na ka and K ka was corrected for Time Dependent Intensity (TDI) loss (or gain) using a self calibrated correction.

At 10 kV the typical detection limits (at the 99% confidence interval) in weight percent were 0.042 for Si, 0.018 for Al, 0.062 for Ti, 0.349 for Fe, 0.258 for Mn, 0.028 for Mg, 0.035 for Ca, 0.035 for Na, 0.036 for K, 0.178 for Ba, and 0.066 for Sr. At 15 k V the typical detection limits (at the 99% confidence interval) in weight percent were 0.035 for Si, 0.013 for Al, 0.027 for Ti, 0.069 for Fe, 0.062 for Mn, 0.016 for Mg, 0.018 for Ca, 0.027 for Na, 0.019 for K, 0.080 for Ba, and 0.049 for Sr. At 20 kV the typical detection limits (at the 99% confidence interval) in weight percent were 0.032 for Si, 0.012 for Al, 0.018 for Ti, 0.037 for Fe, 0.034 for Mn, 0.013 for Mg, 0.013 for Ca, 0.027 for Na, 0.014 for K, 0.052 for Ba, and 0.041 for Sr.

The error on formula unit concentrations was determined by propagating the analytical uncertainty through calculations of structural formulae (Giaramita and Day, 1990).

APPENDIX C. SUPPLEMENTARY DATA

Supplementary data associated with this article can be found, in the online version, at http://dx.doi.org/10.1016/j.gca.2012.06.029.

REFERENCES

Arnould O. and Hild F. (2003) Specific effects and deconvolution in submicrometre EPMA: application to binary diffusion. *X-Ray Spectrom.* **32**, 345–362.

Bachmann O., Oberli F., Dungan M. A., Meier M., Mundil R. and Fischer H. (2007) ^{40}Ar/^{39}Ar and U–Pb dating of the Fish Canyon magmatic system, San Juan Volcanic field, Colorado: evidence for an extended crystallization history. *Chem. Geol.* **236**, 134–166.

Boven A., Pasteels P., Kelley S. P., Punzalan L., Bingen B. and Demaiffe D. (2001) ^{40}Ar/^{39}Ar study of plagioclases from the Rogaland anorthosite complex (SW Norway); an attempt to understand argon ages in plutonic plagioclase. *Chem. Geol.* **176**, 105–135.

Calzolaio M., Arzilli F. and Carroll M. R. (2010) Growth rate of alkali feldspars in decompression-induced crystallization experiments in a trachytic melt of the Phlegraean Fields (Napoli, Italy). *Eur. J. Mineral.* **22**, 485–493.

Cherniak D. J. (2002) Ba diffusion in feldspar. *Geochim. Cosmochim. Acta* **66**, 1641–1650.

Christensen J. N. and Depaolo D. J. (1993) Time scales of large volume silicic magma systems – Sr isotopic systematics of phenocrysts and glass from the Bishop Tuff, Long Valley, California. *Contrib. Mineral. Petrol.* **113**, 100–114.

Clay P. L., Kelley S. P., Sherlock S. C. and Barry T. L. (2011) Partitioning of excess argon between alkali feldspars and glass in a young volcanic system. *Chem. Geol.* **289**, 12–30.

Coombs M. L., Eichelberger J. C. and Rutherford M. J. (2000) Magma storage and mixing conditions for the 1953–1974 eruptions of Southwest Trident Volcano, Katmai National Park, Alaska. *Contrib. Mineral. Petrol.* **140**, 99–118.

Costa F., Chakraborty S. and Dohmen R. (2003) Diffusion coupling between trace and major elements and a model for calculation of magma residence times using plagioclase. *Geochim. Cosmochim. Acta* **67**, 2189–2200.

Costa F. and Chakraborty S. (2004) Decadal time gaps between mafic intrusion and silicic eruption obtained from chemical zoning patterns in olivine. *Earth Planet. Sci. Lett.* **227**, 517–530.

Costa F. and Dungan M. (2005) Short time scales of magmatic assimilation from diffusion modeling of multiple elements in olivine. *Geology* **33**, 837–840.

Crank J. (1975) *The Mathematics of Diffusion*. Oxford, p. 421.

Davies G. R., Halliday A. N., Mahood G. A. and Hall C. M. (1994) Isotopic constraints on the production-rates, crystallization histories and residence times of pre-caldera silic magmas, Long Valley, California. *Earth Planet. Sci. Lett.* **125**, 17–37.

Ebinger C. J., Deino A. L., Drake R. E. and Tesha A. L. (1989) Chronology of volcanism and rift basin propagation - Rungwe volcanic province, east-Africa. *J. Geophys. Res. Solid Earth Planets* **94**, 15785–15803.

Elkins L. T. and Grove T. L. (1990) Ternary feldspar experiments and thermodynamic models. *Am. Mineral.* **75**, 544–559.

Esser R. P., McIntosh W. C., Heizler M. T. and Kyle P. R. (1997) Excess argon in melt inclusions in zero-age anorthoclase feldspar from Mt. Erebus, Antarctica, as revealed by the ^{40}Ar/^{39}Ar method. *Geochim. Cosmochim. Acta* **61**, 3789–3801.

Foland K. A. (1974) ^{40}Ar diffusion in homogeneous orthoclase and an interpretation of Ar diffusion in k-feldspars. *Geochim. Cosmochim. Acta* **38**, 151–166.

Ganguly J., Bhattacharya R. N. and Chakraborty S. (1988) Convolution effect in the determination of compositional profiles and diffusion-coefficients by microprobe step scans. *Am. Mineral.* **73**, 901–909.

Ghiorso M. S. and Sack R. O. (1995) Chemical mass-transfer in magmatic processes.4. A revised and internally consistent thermodynamic model for the interpolation and extrapolation of liquid–solid equilibria in magmatic systems at elevated-temperatures and pressures. *Contrib. Mineral. Petrol.* **119**, 197–212.

Giaramita M. J. and Day H. W. (1990) Error propagation in calculations of structural formulas. *Am. Mineral.* **75**, 170–182.

Gillespie A. R., Huneke J. C. and Wasserburg G. J. (1982) An assessment of ^{40}Ar–^{39}Ar dating of incompletely degassed xenoliths. *J. Geophys. Res.* **87**, 9247–9257.

Gillespie A. R., Huneke J. C. and Wasserburg G. J. (1983) Eruption age of a pleistocene basalt from ^{40}Ar–^{39}Ar analysis of partially degassed xenoliths. *J. Geophys. Res.* **88**, 4997–5008.

Gillespie A. R., Huneke J. C. and Wasserburg G. J. (1984) Eruption age of a approximately 100,000-year-old basalt from ^{40}Ar–^{39}Ar analysis of partially degassed xenoliths. *J. Geophys. Res.* **89**, 1033–1048.

Ginibre C., Worner G. and Kronz A. (2004) Structure and dynamics of the Laacher See magma chamber (Eifel, Germany) from major and trace element zoning in sanidine: a cathodo-luminescence and electron microprobe study. *J. Petrol.* **45**, 2197–2223.

Huber C., Cassata W. S. and Renne P. R. (2011) A lattice Boltzmann model for noble gas diffusion in solids: the importance of domain shape and diffusive anisotropy and implications for thermochronometry. *Geochim. Cosmochim. Acta* **75**, 2170–2186.

Icenhower J. and London D. (1996) Experimental partitioning of Rb, Cs, Sr, and Ba between alkali feldspar and peraluminous melt. *Am. Mineral.* **81**, 719–734.

Jercinovic M. J., Williams M. L. and Lane E. D. (2008) In-situ trace element analysis of monazite and other fine-grained accessory minerals by EPMA. *Chem. Geol.* **254**, 197–215.

Jones D. A., Layer P. W. and Newberry R. J. (2008) A 3100-year history of argon isotopic and compositional variation at El Chichon volcano. *J. Volcanol. Geoth. Res.* **175**, 427–443.

Ketcham R. A. and Carlson W. D. (2001) Acquisition, optimization and interpretation of X-ray computed tomographic imagery: applications to the geosciences. *Comput. Geosci.* **27**, 381–400.

Layer P. W. and Gardner J. E. (2001) Excess argon in Mount St. Helens plagioclase as a recorder of magmatic processes. *Geophys. Res. Lett.* **28**, 4279–4282.

Le Bas M. J., Lemaitre R. W., Streckeisen A. and Zanettin B. (1986) A chemical classification of volcanic-rocks based on the total alkali silica diagram. *J. Petrol.* **27**, 745–750.

Lenoir J. L., Liegeois J. P., Theunissen K. and Klerkx J. (1994) The Palaeoproterozoic Ubendian shear belt in Tanzania – geochronology and structure. *J. Afr. Earth Sci.* **19**, 169–184.

Long P. E. (1978) Experimental determination of partition-coefficients for Rb, Sr, and Ba between alkali feldspar and silicate liquid. *Geochim. Cosmochim. Acta* **42**, 833–846.

Lovera O. M., Grove M., Harrison T. M. and Mahon K. I. (1997) Systematic analysis of K-feldspar ^{40}Ar/^{39}Ar step heating results.1. Significance of activation energy determinations. *Geochim. Cosmochim. Acta* **61**, 3171–3192.

Mahood G. A. and Stimac J. A. (1990) Trace-element partitioning in pantellerites and trachytes. *Geochim. Cosmochim. Acta* **54**, 2257–2276.

Morgan D. J. and Blake S. (2006) Magmatic residence times of zoned phenocrysts: introduction and application of the binary element diffusion modelling (BEDM) technique. *Contrib. Mineral. Petrol.* **151**, 58–70.

Morgan D. J., Blake S., Rogers N. W., DeVivo B., Rolandi G., Macdonald R. and Hawkesworth C. J. (2004) Time scales of crystal residence and magma chamber volume from modelling of diffusion profiles in phenocrysts: Vesuvius 1944. *Earth Planet. Sci. Lett.* **222**, 933–946.

Morgan D. J., Blake S., Rogers N. W., De Vivo B., Rolandi G. and Davidson J. P. (2006) Magma chamber recharge at Vesuvius in the century prior to the eruption of AD 79. *Geology* **34**, 845–848.

Nakamura M. (1995) Continuous mixing of crystal mush and replenished magma in the ongoing Unzen eruption. *Geology* **23**, 807–810.

Njau J. K. and Hlusko L. J. (2010) Fine-tuning paleoanthropological reconnaissance with high-resolution satellite imagery: the discovery of 28 new sites in Tanzania. *J. Hum. Evol.* **59**, 680–684.

Nomade S., Renne P. R., Vogel N., Deino A. L., Sharp W. D., Becker T. A., Jaouni A. R. and Mundil R. (2005) Alder Creek sanidine (ACs-2): a quaternary ^{40}Ar/^{39}Ar dating standard tied to the Cobb Mountain geomagnetic event. *Chem. Geol.* **218**, 315–338.

Philpotts J. A. and Schnetzler C. C. (1970) Phenocryst–matrix partition coefficients for K, Rb, Sr and Ba, with applications to anorthosite and basalt genesis. *Geochim. Cosmochim. Acta* **34**, 307–322.

Putirka K. D. (2008). Thermometers and barometers for volcanic systems. In *Minerals, Inclusions and Volcanic Processes, Reviews in Mineralogy and Geochemistry*, vol. 69 (eds. K. D. Putirka and F. J. Tepley III). pp. 61–120.

Quidelleur X., Gillot P. Y., Soler V. and Lefevre J. C. (2001) K/Ar dating extended into the last millennium: application to the youngest effusive episode of the Teide volcano (Spain). *Geophys. Res. Lett.* **28**, 3067–3070.

Renne P. R. and Norman E. B. (2001) Determination of the half-life of ^{37}Ar by mass spectrometry. *Phys. Rev. C*, 63.

Renne P. R., Sharp W. D., Deino A. L., Orsi G. and Civetta L. (1997) ^{40}Ar/^{39}Ar dating into the historical realm: Calibration against Pliny the Younger. *Science* **277**, 1279–1280.

Renne P. R., Swisher C. C., Deino A. L., Karner D. B., Owens T. L. and DePaolo D. J. (1998) Intercalibration of standards, absolute ages and uncertainties in ^{40}Ar/^{39}Ar dating. *Chem. Geol.* **145**, 117–152.

Renne P. R., WoldeGabriel G., Hart W. K., Heiken G. and White T. D. (1999) Chronostratigraphy of the Miocene-Pliocene Sagantole Formation, Middle Awash Valley, Afar rift, Ethiopia. *Geol. Soc. Am. Bull.* **111**, 869–885.

Renne P. R., Knight K. B., Nomade S., Leung K. N. and Lou T. P. (2005) Application of deuteron–deuteron (D–D) fusion neutrons to ^{40}Ar/^{39}Ar geochronology. *Appl. Radiat. Isot.* **62**, 25–32.

Renne P. R., Sharp Z. D. and Heizler M. T. (2008) Cl-derived argon isotope production in the CLICIT facility of OSTR reactor and the effects of the Cl-correction in ^{40}Ar/^{39}Ar geochronology. *Chem. Geol.* **255**, 463–466.

Renne P. R., Cassata W. S. and Morgan L. E. (2009) The isotopic composition of atmospheric argon and ^{40}Ar/^{39}Ar geochronology: time for a change? *Quat. Geochronol.* **4**, 288–298.

Renne P. R., Mundil R., Balco G., Min K. W. and Ludwig K. R. (2010) Joint determination of ^{40}K decay constants and $^{40}Ar^*/^{40}K$ for the Fish Canyon sanidine standard, and improved accuracy for $^{40}Ar/^{39}Ar$ geochronology. *Geochim. Cosmochim. Acta* **74**, 5349–5367.

Renne P. R., Balco G., Ludwig K. R., Mundil R. and Min K. (2011) Response to the comment by W.H. Schwarz et al. on " Joint determination of ^{40}K decay constants and $^{40}Ar^*/^{40}K$ for the Fish Canyon sanidine standard, and improved accuracy for $^{40}Ar/^{39}Ar$ geochronology " by P.R. Renne et al. (2010). *Geochim. Cosmochim. Acta* **75**, 5097–5100.

Shuster D. L., Flowers R. M. and Farley K. A. (2006) The influence of natural radiation damage on helium diffusion kinetics in apatite. *Earth Planet. Sci. Lett.* **249**, 148–161.

Singer B. S., Dungan M. A. and Layne G. D. (1995) Textures and Sr, Ba, Mg, Fe, K and Ti compositional profiles in volcanic plagioclase – clues to the dynamics of calc–alkaline magma chambers. *Am. Mineral.* **80**, 776–798.

Singer B. S., Wijbrans J. R., Nelson S. T., Pringle M. S., Feeley T. C. and Dungan M. A. (1998) Inherited argon in a Pleistocene andesite lava: $^{40}Ar/^{39}Ar$ incremental-heating and laser-fusion analyses of plagioclase. *Geology* **26**, 427–430.

Solomatov V. S. (1995) Batch crystallization under continuous cooling – analytical solution for diffusion-limited crystal-growth. *J. Cryst. Growth* **148**, 421–431.

Stoenner R. W., Schaeffer O. A. and Katcoff S. (1965) Half-lives of argon-37 argon-39 and argon-42. *Science* **148**, 1325–1328.

Wartho J. A., Kelley S. P., Brooker R. A., Carroll M. R., Villa I. M. and Lee M. R. (1999) Direct measurement of Ar diffusion profiles in a gem-duality Madagascar K-feldspar using the ultra-violet laser ablation microprobe (UVLAMP). *Earth Planet. Sci. Lett.* **170**, 141–153.

Zeitler P. K. (1987) Argon diffusion in partially outgassed alkali feldspars - insights from $^{40}Ar/^{39}Ar$ analysis. *Chem. Geol.* **65**, 167–181.

Zellmer G. F. and Clavero J. E. (2006) Using trace element correlation patterns to decipher a sanidine crystal growth chronology: an example from Taapaca volcano, Central Andes. *J. Volcanol. Geoth. Res.* **156**, 291–301.

Associate editor: Peter Reiners